Available online at www.sciencedirect.com
ScienceDirect
Trans. Nonferrous Met. Soc. China 33(2023) 168−188
Transactions of Nonferrous Metals Society of China
www.tnmsc.cn

Optimization of microstructure and properties of laser sintered $Ni_{30}Cr_{25}Al_{15}Co_{15}Mo_5Ti_5Y_5$ high-entropy alloy coatings via controlling plasma

Xue YAN[1], Jian-yan XU[2], Xiang-he GUAN[3], Bing-yuan HAN[4], Cheng ZHANG[1], Zi-ruo CUI[5], Wen-ping LIANG[2]

1. State Key Laboratory of High Field Laser Physics, Shanghai Institute of Optics and Fine Mechanics, Chinese Academy of Sciences, Shanghai 201800, China;
2. Department of Material Science and Technology, Nanjing University of Aeronautics and Astronautics, Nanjing 211106, China;
3. Shanghai Institute of Laser Plasma, China Academy of Engineering Physics (CAEP), Shanghai 201800, China;
4. School of Automotive and Traffic Engineering, Jiangsu University of Technology, Changzhou 213001, China;
5. Key Laboratory for Laser Plasmas (MOE), Collaborative Innovation Center of IFSA (CICIFSA), School of Physics and Astronomy, Shanghai Jiao Tong University, Shanghai 200240, China

Received 15 October 2021; accepted 28 March 2022

Abstract: An active suppressing method of laser-induced plasma was proposed to optimize the crystal structure and tribological properties for the surface laser sintering (SLS) of $Ni_{30}Cr_{25}Al_{15}Co_{15}Mo_5Ti_5Y_5$ high-entropy alloy (HEA) coatings using a pulsed laser with various shielding gases. The results indicate that electron temperature (T_e) and the plasma jet volume with no shielding gas or in He atmosphere were higher than those in Ar−He atmosphere. Well-defined phase transitions and significant metal atom diffusion occurred in SLS, and metallurgical bonding occurred with the precipitation of α-$AlFe_3$, α-AlNi, and γ-$AlFe_2Ni$. The lower energy absorbed by the plasma via inverse bremsstrahlung (IB) strengthened interactions between laser and HEA, increasing the microhardness, and reducing the dynamic friction coefficient. This elucidates the crucial influence of plasma control on laser-based additive manufacturing.

Key words: laser-induced plasma; surface laser sintering (SLS); electron temperature (T_e); inverse bremsstrahlung absorption (IB); high-entropy alloy (HEA); residual stress

1 Introduction

In high-energy physics and super-intense laser facilities, the pipeline pressure vessel, a kind of closed vessel which can bear pressure, is commonly used to realize the transmission of the super-intense beam [1,2]. To ensure ease of laser beam transmission for reducing the impact of high-energy laser beams, the light-transmission pipeline should reach a very high vacuum degree, which places strict requirements on the surface mechanics and wear behavior of the pipeline pressure vessel.

High-entropy alloy (HEA) superalloys are not easy to precipitate harmful phases [3−5] compared with Fe-based superalloys, and can work at high temperature and high stress environment, which can greatly enhance the high-temperature mechanical properties, friction and wear properties of optical transmission pipe. The crystal structure of HEAs has a large influence on the tensile properties [6]. The $Al_{0.3}CoCrFeNi$ HEA at low temperature has good plastic-deformation behavior for the formation of deformation twins, which is similar to

Corresponding author: Xiang-he GUAN, E-mail: guanxianghe@163.com
DOI: 10.1016/S1003-6326(22)66098-9

the CoCrFeMnNi alloy studied by OTTO et al [7]. Moreover, it was found that CoCrFeMnNi HEA maintained the face-centered cubic single-phase structure after high intensity pulsed ion beam irradiation [8]. ZHANG et al [9] reviewed the recent development of HEAs, and summarized the preparation methods and composition design.

Laser sintering has unique advantages in interacting with powder or sheet compacts which are different from substrate for difficult-to-machine parts with high requirements [10−12]. Emerging micro additive manufacturing technologies enabled by novel optical methods has attracted the attention of researchers [13,14], and ultrafine micro nanostructures can be prepared by ultrafast laser [15,16]. AIZENSHTEIN et al [17] investigated the effect of pre-deformation and *B*2 morphology on the mechanical properties of Al0.5CoCrFeNi HEA, showing that deformation prior to heat treatment can alter the *B*2 phase morphology from "plate-like" to equiaxed morphology. ERDOGAN and DOLEKER [18] reported that Al0.2CrFeNiCo and Al0.2CrFeNiCu high entropy alloys were deposited with high velocity oxygen fuel (HVOF) on 316L substrate, and found that laser re-melting coatings exhibited better oxidation performance. Moreover, GERA et al [19] compared the properties of Cu−Al−Ni−Mn−Zr shape memory alloy prepared by selective laser melting and conventional powder metallurgy. However, the influence of laser-induced plasma plume and refractive index of lens affected by temperature should be examined in the process of high power laser interaction with materials [20−22]. Laser parameters and processing environment are thought to be the two major factors affecting the plasma, which attracts many scholars interests in studying the laser-induced plasma process. Pulse contrast is the key parameter of high peak-power lasers since the prepulse noise may disturb laser−plasma interactions [23,24]. According to the acoustic emission (AE) signals, LUO et al [25] studied the characteristics of plasma plume and penetration of weld bead and found that the source for AE generation was the recoil force and thermal vibration generated by the plasma plume acting on molten pool. WU et al [26] proposed that the cooling effect, blowing effect and the static pressure were enhanced by the lateral restraint, and the restraint effect of the nearwall low-temperature area limited the expansion of the plasma plume greatly. During the laser welding of titanium alloy, ZHANG et al [27] found that the periodic variations of the keyhole area (KA) and the centroid high plasma plume (CHPP) are unstable and the laser power of 1000 W is a turning point and affects the variation trends of the KA and the CHPP. JIANG et al [28] found that the decrease of plasma plume disturbance, the increase of the laser energy in keyhole and the decrease of boiling temperature changed the absorption mechanism of laser energy, resulting in a large aspect ratio with narrow and parallel sides of weld cross section profile under vacuum. However, they have not discussed the processing of the interaction between laser and matter in depth.

In Cantor alloy and $Al_xCoCrFeNi$ HEAs system, adding Ti, Mo and Y can be easy to form phase structures with FCC, BCC and HCP solid-solution structures [9]. So, the $Ni_{30}Cr_{25}Al_{15}Co_{15}$-$Mo_5Ti_5Y_5$ HEA coatings were prepared on P355GH via surface laser sintering (SLS) under different working modes of pulsed/CW lasers in the atmosphere to improve the surface performance of pressurized light-transmission pipes in this study. The effect of laser-induced plasma on SLS was investigated by analyzing the micromechanics, friction, and wear behavior of the HEA coatings.

2 Experimental

The HEA coatings were prepared via SLS with a custom robotic laser workcell (IPG Photonics Corporation) which employed YLS−10000 laser. The SLS system and cycle strengthening are shown in Fig. 1. The SLS parameters are given in Table 1. To study the interaction of the plasma plume with the laser beam, a NAC high-speed camera (20 kHz) was used to capture the morphology of the plasma plume. A schematic diagram of the laser-induced plasma is illustrated in Fig. 1.

The chemical compositions of P355GH structural steel as the substrate are given in Table 2. The surface of the P355GH steel was finished and soaked in acetone for 30 min to remove oil, dust and other impurities. Then, the substrate was sandblasted to remove the oxide layer, and the coating was prepared within 2 h.

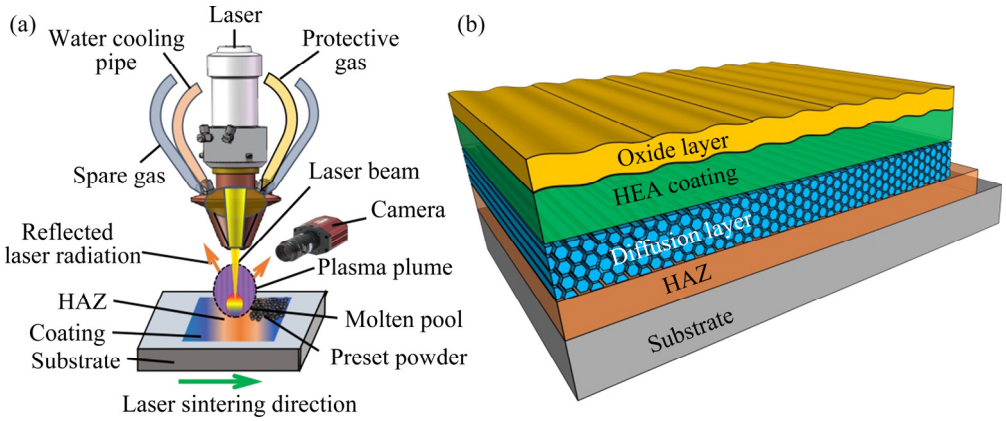

Fig. 1 SLS system (a) and HEA coating (b)

Table 1 Parameters employed in SLS process

Parameter	Value
Focal length/mm	400
Defocusing amount/nm	600
Laser wavelength/nm	1070±5
Spot diameter/mm	3
Particle size/μm	23−74
Laser sintering distance/mm	900
Scanning speed/(mm·s^{-1})	2
Overlap ratio/%	50
Gas velocity/(L·min^{-1})	6
Fiber core diameter/μm	100

Table 2 Chemical compositions of P355GH structural steel (wt.%)

Mn	Si	Cr	Cu	Ni	Mo
1.10−1.70	≤0.60	≤0.30	≤0.30	≤0.30	≤0.08
Nb	Ti	V	Impurity	Fe	
≤0.04	≤0.03	≤0.02	≤0.257	Bal.	

The sintering powder presented on the substrate by squash presetting method was precipitation strengthening high-entropy alloy powder with spherical structure prepared by aerosol method and the presetting thickness was ~1 mm, with particle size of 50−200 μm. The chemical compositions of high-entropy alloy powder are given in Table 3. The most important role of Cr in high-entropy alloy powder was to increase the oxidation resistance and wear resistance. Al and Ti are critical elements to improve the surface stability of the alloy. It is generally believed that high Al is conducive to improving the oxidation resistance of the alloy [29]. Increasing the content of Al results in the formation of a BCC phase in the FCC matrix, which yields an increase in the compressive strength at the expense of ductility [30,31]. The Ti was conducive to improving the hot corrosion resistance, and a BCC structure was formed within the FCC solid-solution phase in Cantor alloy (containing Fe-BCC, Co-HCP, Cr-BCC, Mn-BCC and Ni-FCC) when Ti-HCP was added [32,33]. Mo can increase the amount of γ phase and improve the thermal stability.

Table 3 Chemical compositions of high-entropy alloy powder (wt.%)

Ni	Cr	Al	Co	Mo	Ti	Y
30.00	25.00	15.00	15.00	5.0	5.00	5.00

According to the influential factors of laser-induced-plasma, different working modes of CW/Modulated and atmospheric environment were used in the SLS process. The working modes of laser and shielding gas, and the corresponding sample number are given in Table 4.

Table 4 Sample number under different working modes and shielding atmospheres

Laser	No shielding gas	He shielding gas	Ar−He shielding gas
Pulse	000	100	110
CW	001	101	111

Before the experiment, the temperature changes for pulsed and CW laser sintering were simulated, as shown in Figs. 2(a, b). During laser

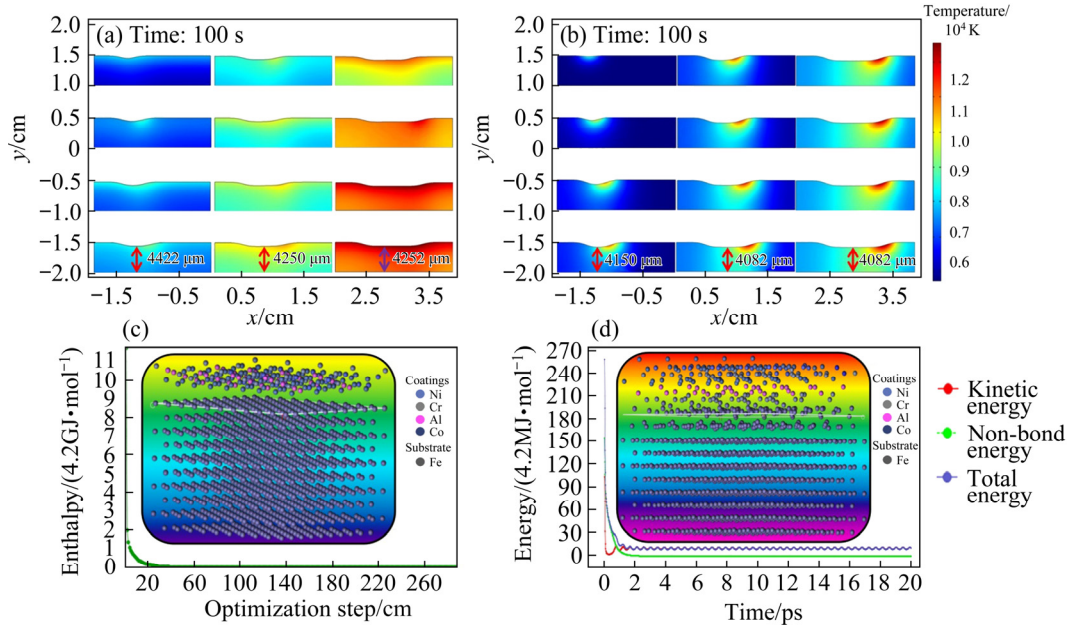

Fig. 2 Macro finite element temperature field and molecular dynamics: (a) Pulsed laser; (b) CW laser; (c) Enthalpy; (d) Energy

scanning, the initial substrate temperature gradually increased under the action of long-time pulse pumping, showing a significant heat accumulation superposition effect [34]. This was the same as the simulation of the pulsed laser power and temperature by SU et al [35], which showed that preheating and reducing the thermal relaxation time can improve the power and efficiency of pulsed lasers. With a laser power of 5 kW, the use of either pulsed (1 kHz in frequency) or CW laser sintering can result in a temperature of 10^4 K in the molten pool center and match the temperature of the induced plasma. Compared with sintering using a pulsed laser, the substrate temperature rise induced by the CW laser was limited to a small area; however, the sintering thickness was much larger than that obtained using the pulsed laser.

A molecular dynamics simulation created with the Forcite module of Materials Studio is shown in Figs. 2(c, d). Molecular mechanics were used to explore the possible structures from several typical structural parameters and forces. A potential energy function was used to express the change in molecular energy when the organizational parameters deviated from the “ideal” value. Additionally, an optimization method was used to determine the change in molecular energy when the molecular energy deviated from the “ideal” value. The optimization method was also used to find the configuration of the molecule when the molecular energy was in the minimum state. According to the ergodic hypothesis in statistical physics, the time average of physical quantities is equal to the average result of all systems in the canonical ensemble (NVT) for a system in equilibrium. The physical properties of the equilibrium state of the system can be obtained by summing different microscopic states. In Fig. 2(d), the Fe in P355GH and the four main elements in the coating built a HEA system, and the molecular dynamics energy and temperature reached dynamic equilibrium in the range of 42−75.6 MJ/mol and 2200−3000 K. Similar to the molecular dynamics simulation of temperature effects, increasing temperature reduced the anisotropy of distribution of atoms, which can be ascribed to the fact that regular registry of surface lattice atoms was changed with the increase of thermal vibration amplitude of surface atoms [36].

The obtained HEA coatings after SLS experiment were polished, and the coating interfaces were slightly corroded by dilute nitric acid, which can be convenient to distinguish coating from substrate. Typical spectrograms between 200 and 600 nm were acquired using a Leetes WL8A-pro spectrometer during the SLS of the HEA under different laser working modes and atmospheres. Morphologies, element compositions

and phases were analyzed using a JSM−6360LA type scanning electron microscope (SEM), energy dispersive spectrometer (EDS), and D/max2500 PC X-ray diffraction (XRD), respectively. Micro-hardness tests under a load of 100 g for 10 s were performed using a HXD−1000TC tester. The residual stress using fixed peak method for cross correlation method conducted on X−350AC stress tester with the Co target, incident angle of 0°, 25°, 35° and 45°, stress constant of −130 MPa/(°), 2θ range of 155°−145° and scanning step of 0.10°. The tensile test was carried out at the tensile rate of 1 mm/min in the air to evaluate the mechanical properties. Finally, the friction experiments were conducted on CETR equipment, using the ball−plane sliding contact mode, with Si_3N_4 ceramic ball as grinding pair with diameter of 3.5 mm, and the load was 10 N.

3 Results and discussion

3.1 Plasma plume

3.1.1 Observations and analysis of plasma plume

The plasma plume and molten pool under different laser working modes and atmospheres are shown in Fig. 3(a). The plasma plumes consisted of ionized metal vapor and ambient gases. Compared with the plasma plumes in laser welding, those induced by SLS stretched in the horizontal direction due to transverse scanning, and the range of the plasma plumes was narrowed as the pattern number increased. Based on the theory of plasma sheath layering, the laser-induced plasma produced by SLS was an electromagnetic fluid filled with high-speed electrons and ions. Both the number and thermal velocity of electrons impacting the probe, were much higher than those of the ions, as the thermal velocity of the electrons was much higher than that of the protons. Based on the principle of potential and a study by REISGEN et al [37], the flow rates of the electrons and ions reach equilibrium, thus forming the plasma sheath layer, as shown in Fig. 3(b).

The potential difference between the probe and sheath edge was U_{PCS} when the particles with dots reached equilibrium at the sheath and the thickness of the plasma sheath was l_s, described as [38]

$$U_{PCS}=\frac{kT}{e}\ln\left(\frac{m_i}{m_e}\right)^{1/2} \tag{1}$$

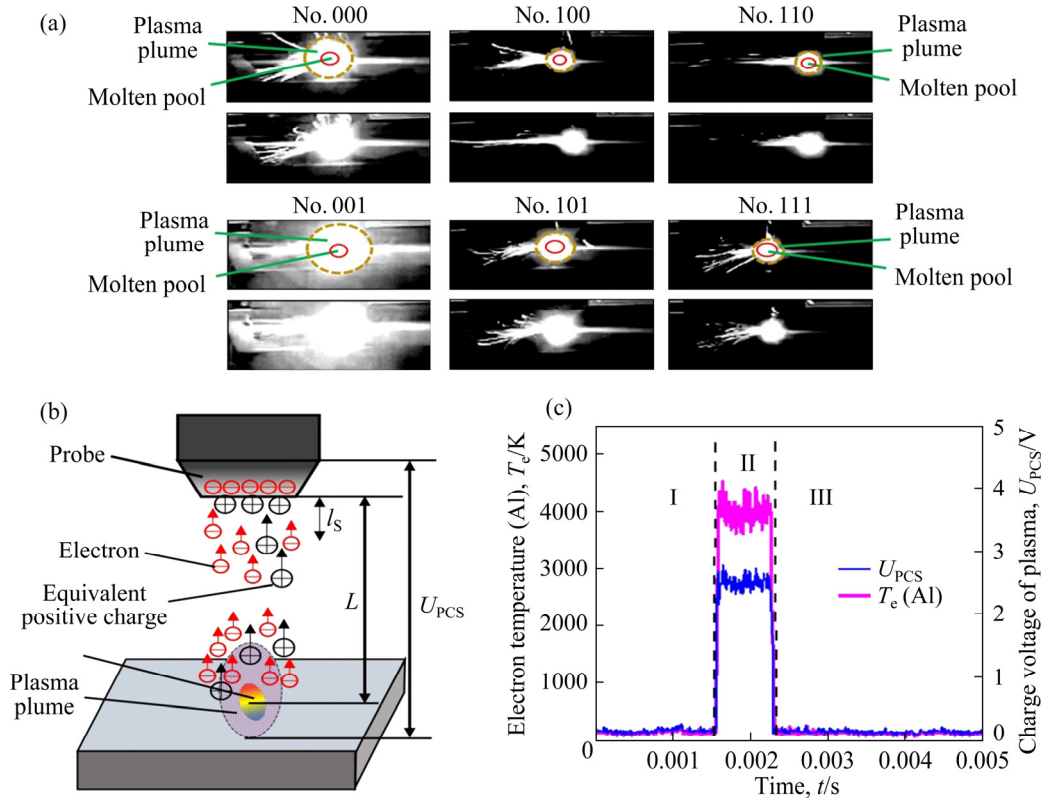

Fig. 3 Induced mechanism of sheath potential in plasma: (a) Plasma plume; (b) Sheath potential; (c) Charge voltage and electron temperature

where k is the Boltzmann constant, T is the temperature, m_i is the ion mass, m_e is the electron mass, and e is the electron charge.

In accordance with the plasma sheath theory and the charge voltage of Ni, the plasma electron temperature (T_e) was calculated, and the signal waveforms of the charge voltage and T_e in the active period of a single plasma are shown in Fig. 3(c). The dynamic behavior of the plasma plume can be divided into three stages: (1) the excitation phase, (2) the maintenance phase, and (3) the decay phase. The charge voltage and T_e of the plasma plume fluctuated within 2−3.0 V and 3000−4000 K, respectively, during the maintenance phase.

3.1.2 Analysis of spectroscopy

The typical spectra from 200 to 600 nm, obtained during the SLS of the HEA coatings under different laser working modes and shielding atmospheres, are shown in Fig. 4. The emission spectra of the laser-induced plasma produced under atmospheric conditions consisted of a broadband background and hundreds of discrete emission lines. The broadband background was caused by the intense thermal radiation of the plasma plume, while the discrete emission lines corresponded to

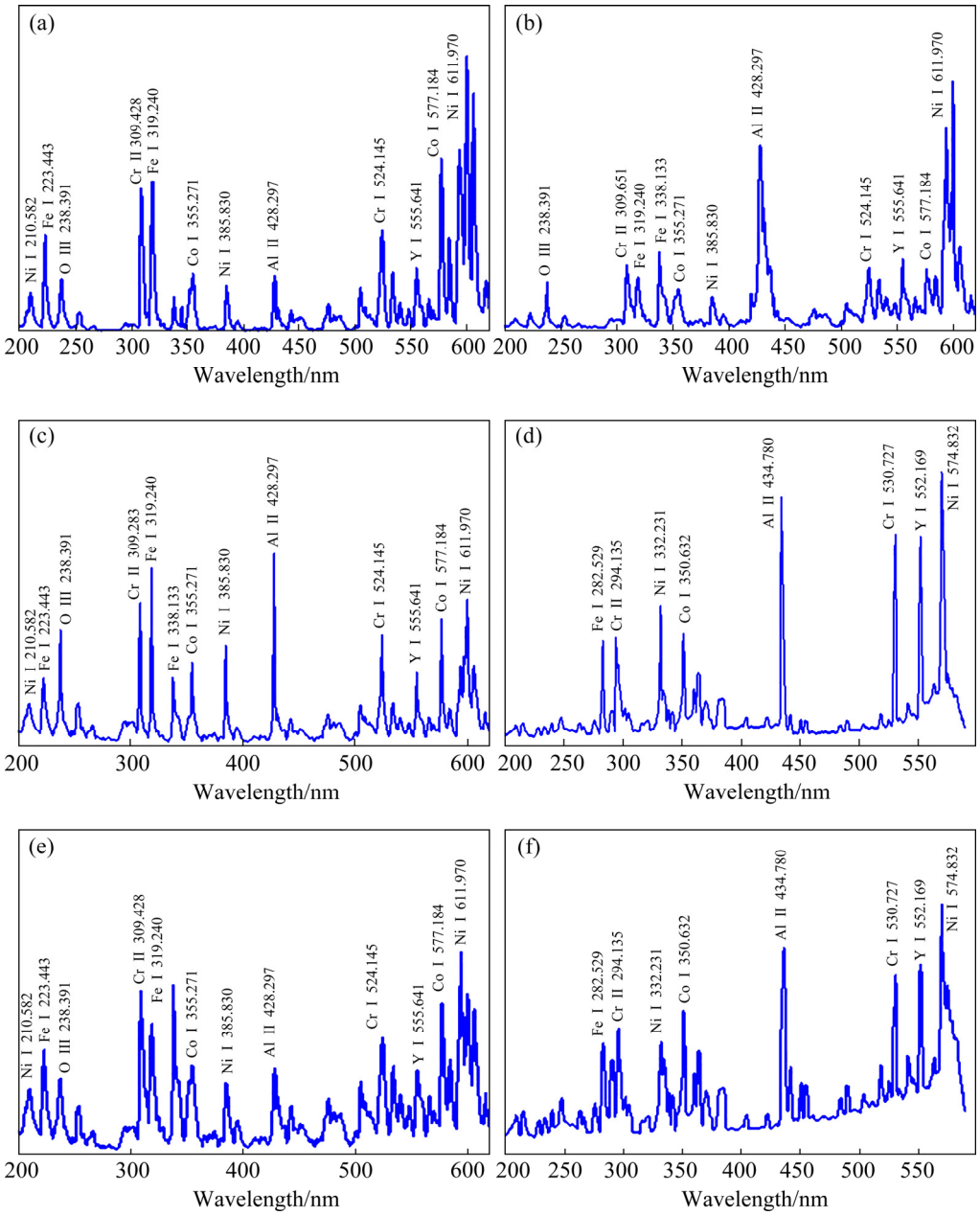

Fig. 4 Typical spectra under different working modes and shielding atmospheres: (a) No. 000; (b) No. 001; (c) No. 100; (d) No. 101; (e) No. 110; (f) No. 111

the spectral lines of the Ni, Cr, Al, Co, and Fe atoms and molecules. Ni was mainly detected near the wavelengths of 333.231, 385.830, and 611.970 nm, Cr near 309.428 and 524.145 nm, Al near 428.297 and 434.780 nm, Co near 355.271 and 577.184 nm, and Fe near 282.529 and 319.240 nm. A low-intensity O signal also appeared in the spectra, except for No. 110 and No. 111, which indicated that some metal atoms were oxidized. Under different working modes and protective atmospheres, some spectral lines disappeared and others appeared, which indicated that the state of the plasma plume in SLS was influenced by the working mode and shielding gas atmosphere. Additionally, the emission intensity of the plasma plume tended to decrease with the pulsed mode and Ar−He shielding gas environment. Meanwhile, the reduction of emission intensity indicated that the thermal radiation of the plasma plume is weakened, due to diversification of the shielding gas atmosphere [39].

3.1.3 Electron temperature, electron density and inverse bremsstrahlung (IB) absorption of plasma

The T_e and electron density (N_e) are critical basic indices to characterize plasma plumes and estimate IB absorption. Taking into account the theory of plasma sheath, in addition to Eq. (1), the electron temperature can be calculated by Eq. (2) under spectral conditions [40−42]:

$$\log\left(\frac{I_{mn}\lambda}{g_m A_{mn}}\right)=-\frac{E_m}{kT_e}+D \tag{2}$$

where I_{mn} is the relative spectral intensity, λ is the wavelength, A_{mn} is the transition probability of spontaneous emission, g_m is the degeneracy of the excitation level, E_m is the upper-state energy level, and D is a constant. By plotting the initial term, $\log[I_{mn}\lambda/(g_m A_{mn})]$, versus E_m for several lines of the same element in the Boltzmann plot, one can estimate the electron temperature T_e, which is related to the slope of the linear fit $-1/(kT_e)$.

N_e can be calculated based on the spectra according to the Stark broadening effect. The formula [43] to estimate the N_e is expressed as

$$N_e=\frac{\Delta\lambda_{1/2}}{2w}\times10^{16} \tag{3}$$

where $\Delta\lambda_{1/2}$ is the full-width at half-maximum (FWHM), and w is the electron collision-broadening half-width. In this study, the line of Ni, I 574.83 nm with high relevancy, was selected to compute N_e.

IB absorption is the main route for plasma to absorb and shield laser energy. The IB linear absorption coefficient can be estimated as [44]

$$A_{ib}=\frac{Z^2e^6n_e n_i\ln\Lambda}{3\omega^2c\varepsilon_0(2\pi m_e kT)^{3/2}\sqrt{1-(\omega_p/\omega)^2}} \tag{4}$$

where A_{ib} is the IB linear absorption coefficient, Z is the ionic valence, n_e is the electron density, n_i is the ions density, $\ln\Lambda$ is the Coulomb logarithm, ω is the angular frequency of the laser, ω_p is the angular frequency of the plasma oscillation, c is the speed of light, and ε_0 is the dielectric constant of vacuum.

According to the interaction mechanism between the laser and plasma plume, the energy flux ratio of the laser through the plasma layer was described by the beam transmittance rate. The relationship between A_{ib} and the plasma length L (measured from the plasma plume images) was established. The obtained transmittance represents the effective power efficiency:

$$Q/Q_0=\exp(-A_{ib}L) \tag{5}$$

where Q is the effective energy and Q_0 is the incident energy of the laser.

The T_e values for a single plasma active cycle and surface metallography of the plasma and HEA coatings are shown in Figs. 5−7. The influence of the working mode and shielding gas on the laser-sintered coatings was characterized by the fluctuations of the electron temperature and plasma. Since plasma can absorb laser energy above the surface of the material, the temperature was increased and the absorption rate of the laser energy by the material was reduced. From the results, it seemed that the plasma induced by laser sintering had a shielding effect on the SLS process. The higher the T_e of the plasma, the more the laser energy absorbed by the plasma, and therefore, the more pronounced the shielding effect. As shown in Fig. 5, T_e without the shielding gas reached 5000 K, and the eruption volume of the plasma plume was noticeably larger than that of other four samples. Compared with the fluctuations between 4000 and 5000 K seen for No. 100 and No. 101, the T_e for No. 110 and No. 111 under Ar−He shielding gas was lower, with fluctuations between 3000 and

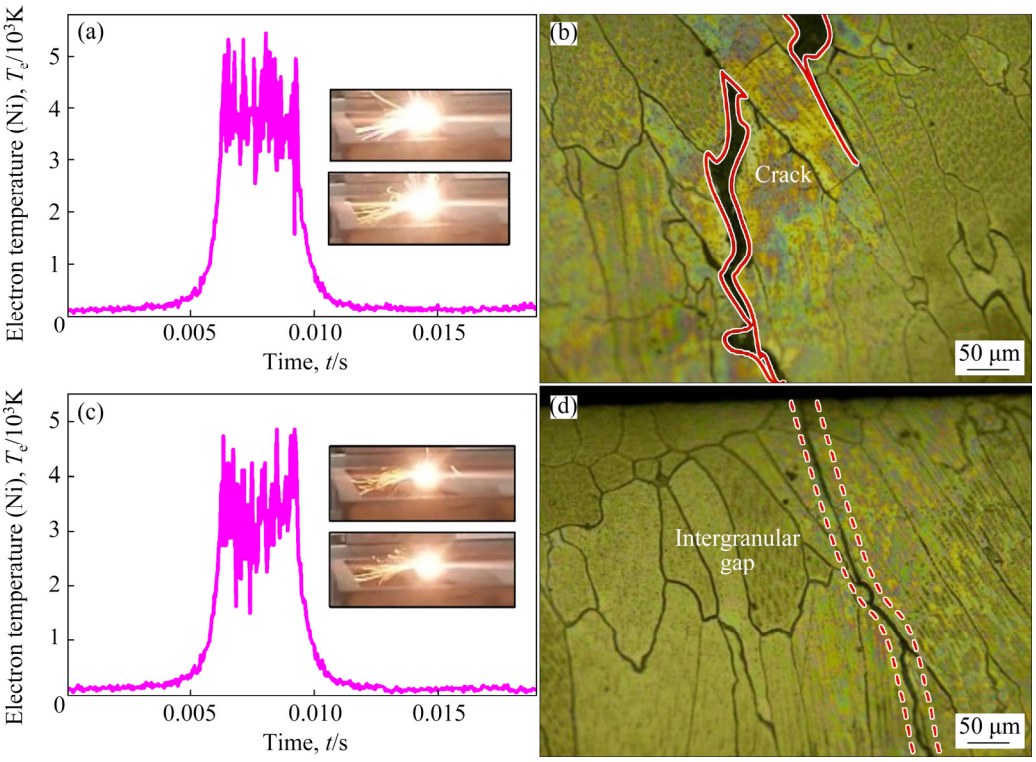

Fig. 5 Electron temperature and surface morphologies of No. 000 (a, b) and No. 001 (c, d)

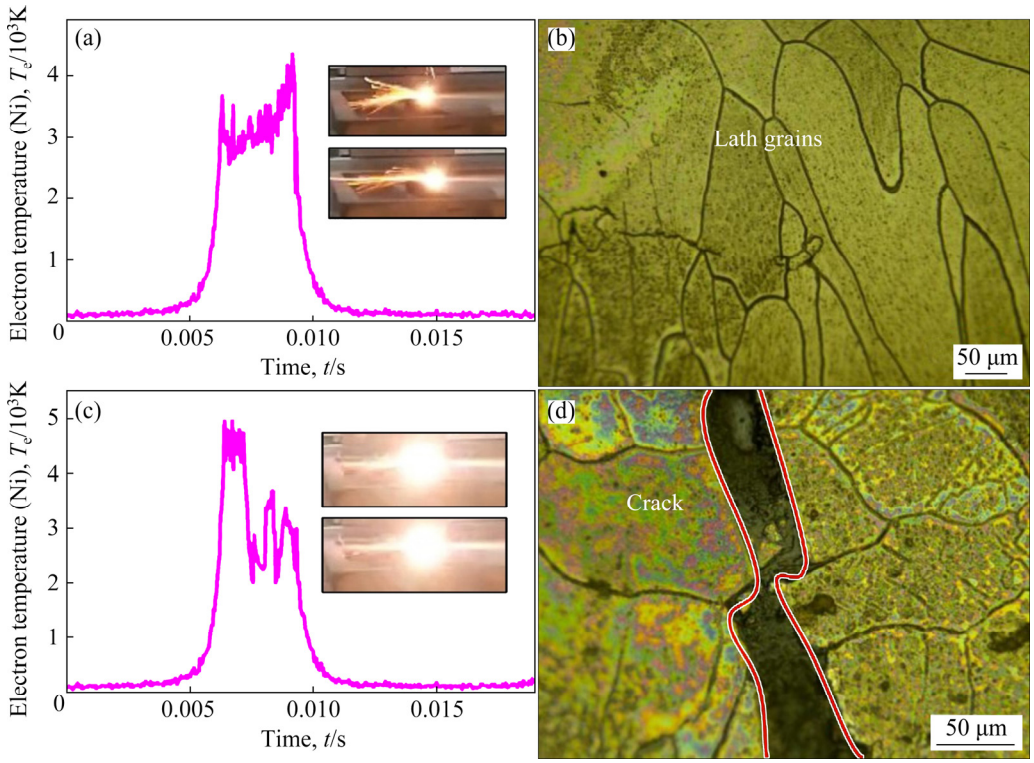

Fig. 6 Electron temperature and surface morphologies of No. 100 (a, b) and No. 101 (c, d)

4000 K. The T_e and jet volume of plasma under He gas were higher than those under Ar−He, which indicated that the shielding effect induced by SLS under various gases followed the order of no shielding gas > He shielding gas > Ar−He shielding gas. Furthermore, by comparing No. 000 with

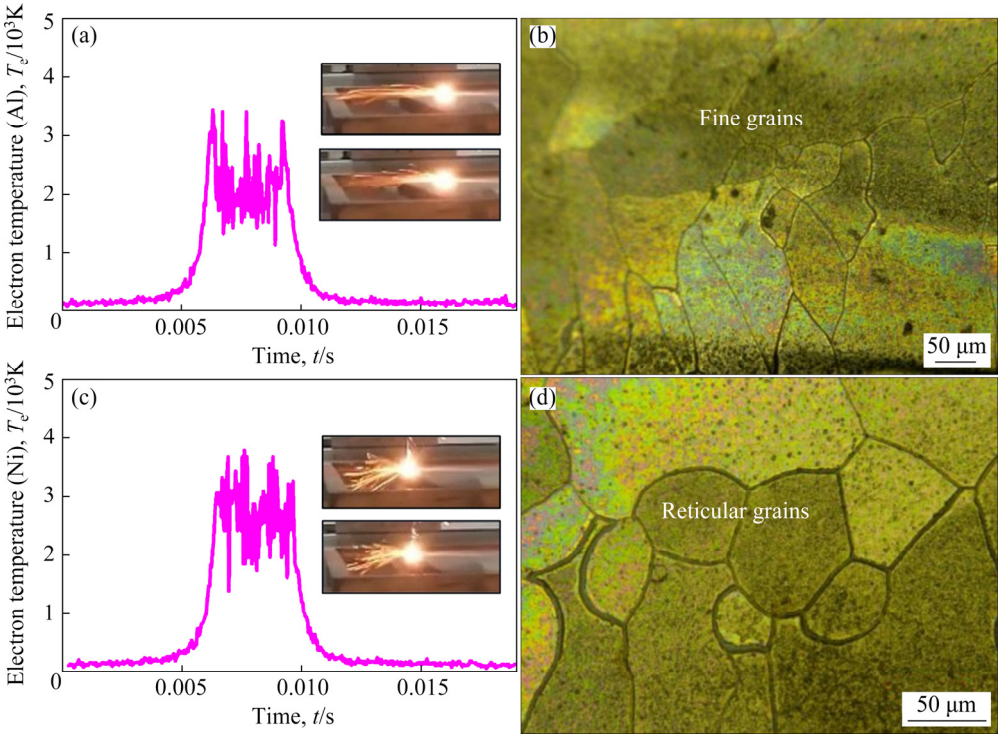

Fig. 7 Electron temperature and surface morphologies of No. 110 (a, b) and No. 111 (c, d)

No. 001, No. 100 with No. 101, and No. 110 with No. 111, it seemed that the T_e using the pulsed laser was lower than that using the CW laser, because the irradiation time of the laser was less than the forming time of the plasma, which was achieved by adjusting the pulse frequency of the laser to inhibit the generation of plasma.

Furthermore, the IB absorption of laser energy by laser-induced plasma had important influence on the quality of the alloy coating. Figure 5 showed clear microcracks on the surface of the two alloy coatings fabricated by SLS without shielding gas, with crack width of 50 and 20 μm, respectively, due to the inhomogeneous thermal effects resulted from the high-intensity laser-induced plasma. Figure 6 showed lath grains on the surface of No. 100 and intergranular gaps on No. 101. Figure 7 showed fine grains on the surface of No. 110 and reticular grains on No. 111. These effects are preliminarily judged to be caused by stress under the influence of the laser-induced plasma.

3.2 Microstructure of HEA coatings

3.2.1 Analysis of coatings surface

The surface morphology and energy dispersive X-ray spectroscopy (EDS) results of the HEA coatings are shown in Fig. 8. The accumulation of surface grains on No. 100 decreased significantly compared with that on No. 101, but the surface grains on No. 101 exhibited significant peeling. The energy absorption of the HEA was inhibited due to the shielding of the laser-induced plasma, corresponding to the T_e of No.101 reaching 5000 K, as can be seen in Fig. 8. There was no distinct grain accumulation or peeling on No. 110 and No. 111. Judged from the Fe content in the EDS results, the diffusion of No. 110 between the coating and substrate was more pronounced, which can also be seen in the line scan of the coating interface. This indicates that the HEA was composed of five major metal elements: Ni, Cr, Al, Co, and Fe.

3.2.2 Analysis of coatings interface

The line scan of the HEA coatings fabricated by SLS is shown in Fig. 9. The coating thicknesses of No. 100, No. 101, No. 110, and No. 111 were ~580, ~600, ~660, and ~600 μm, and the thicknesses of the heat-affected zone (HAZ) were ~400, ~220, ~260, and ~240 μm, respectively. The Ni, Cr, Al, Co, and Fe underwent distinct content changes at the coating interface, as each element content fluctuated across a region near the junction of the alloy coatings and HAZ, referred to as the diffusion zone. The diffused thicknesses of No. 101 ranged from 180 to 220 μm, those of No. 100 and

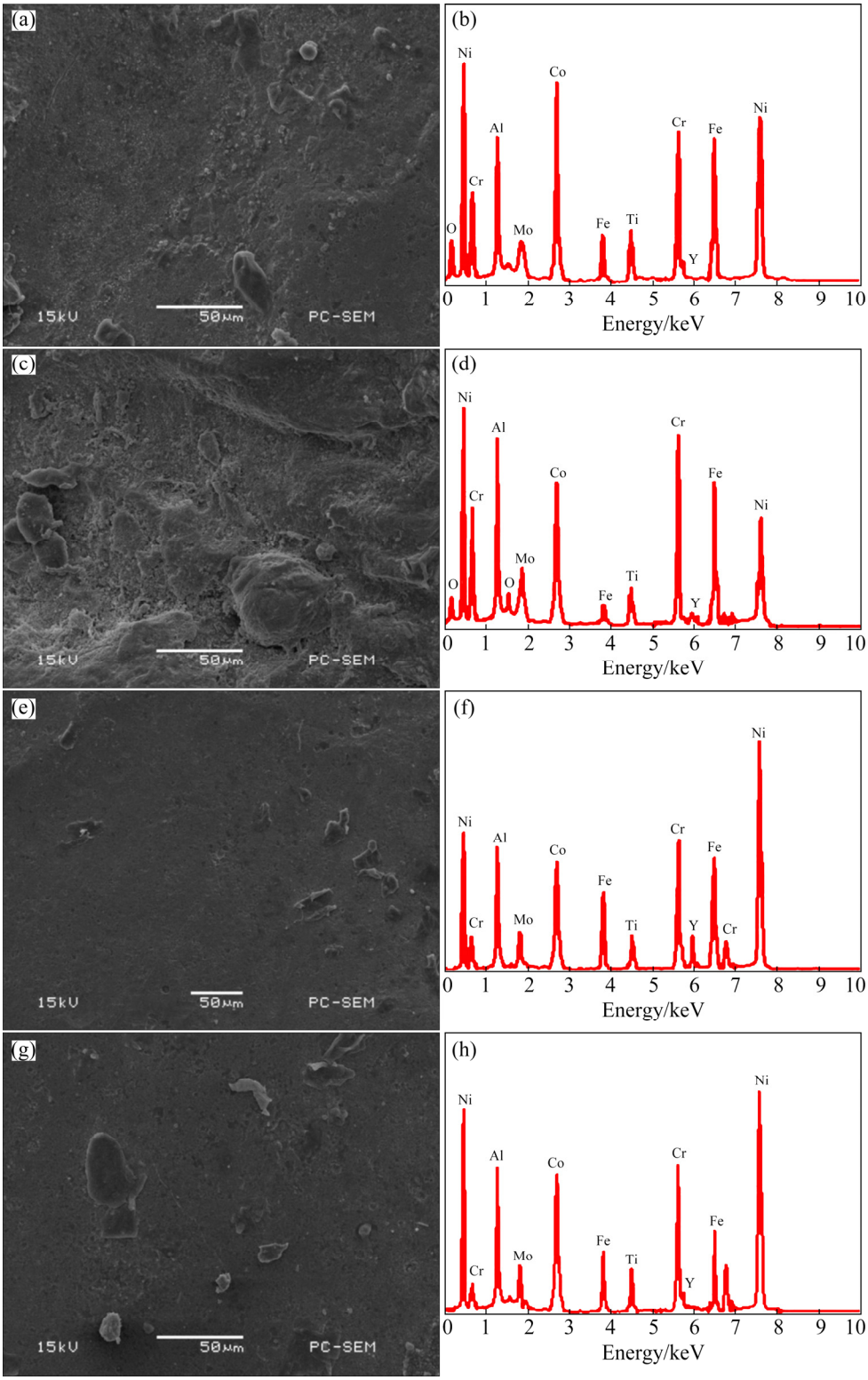

Fig. 8 SEM images and EDS results of HEA coatings under different working modes and shielding atmospheres: (a, b) No. 100; (c, d) No. 101; (e, f) No. 110; (g, h) No. 111

No. 111 ranged from 50 to 60 μm, and only that of No. 110 approached 300 μm. These values indicate that there occurred considerable interdiffusion and metallurgical bonding between the P355GH steel and alloy coatings, due to the mutual transfer of atoms and molecules. The more pronounced the diffusion changes, the greater the penetration depth and dilution ratio are.

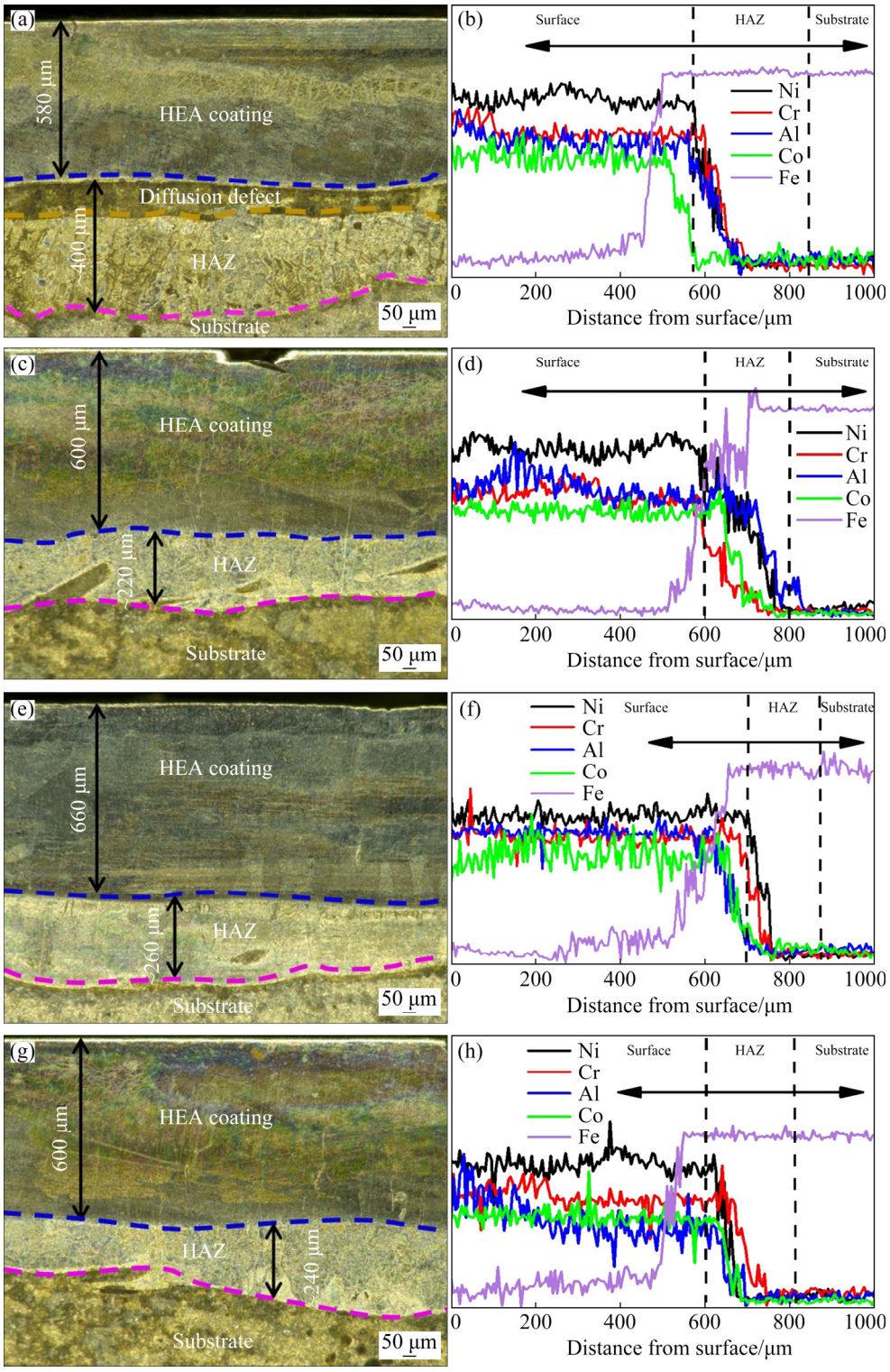

Fig. 9 Interface morphologies and compositions of HEA coating under different working modes and shielding atmospheres: (a, b) No. 100; (c, d) No. 101; (e, f) No. 110; (g, h) No. 111

3.2.3 Thermodynamics and phase transition of HEA coatings

The energy deposition from SLS depended on the repetition rate and sintering speed of SLS, which defined the relationship between the pulse frequency and thermal diffusion time. The results indicate that the temperature limit was positively influenced by the number of pulses, and the heat accumulation effect was significant. It is well known that the thermal accumulation effect is a

prominent feature when using CW lasers.

Suppressing the thermal effect of SLS will allow control of the latent heat of liquefaction, which can lead to phase transformations between the HEA coatings and P355GH. The phases of the HEA coatings prepared using SLS under various working modes and shielding atmospheres are shown in Fig. 10. The main peaks of the stable phases γ-$AlFe_2Ni$ (JCPDS No. 44-1126), α-AlNi (JCPDS No. 44-1187), NiCoCrMo (JCPDS No. 35-1489), and α-FeNi (JCPDS No. 47-1417) were detected at 2θ=31.38°, 44.34°, 50.36°, and 81.16°, respectively. The combination of the Fe in the P355GH steel with the Ni and Al in the alloy coatings indicates that significant phase transitions and metal atom diffusion occurred during SLS. Furthermore, low-intensity diffraction peaks of Cr_2O_3 (JCPDS No. 84-0315), α-$FeNi_3$ (JCPDS No. 38-0419), α-$AlFe_3$ (JCPDS No. 45-1204), NiO (JCPDS No. 44-1159), and α-Al_2O_3 (JCPDS No. 29-0063) were detected at 2θ=19.78°, 42.54°, 64.60°, 74.18°, and 89.76°, respectively, indicating the presence of crystalline oxidation phases. In addition, the spectral intensities of Cr_2O_3 and α-Al_2O_3 gradually decreased, from No. 000 and No. 100 to No. 110 and from No. 001 and No. 101 to No. 111, respectively. The mutual diffusion at the coating interface yielded new phases, enhancing the bonding strength and elastic modulus according to the Gibbs phase rule. The Al−Ni and Al−Fe−Ni phases helped form phase structures with the FCC, BCC and HCP solid-solution and alloy compounds structures, which can increase the bonding strength and microhardness of the coating. Therefore, the friction and wear properties of structural steel surface can also be greatly improved.

3.3 Mechanical properties of HEA coatings

3.3.1 Microhardness and residual stresses of HEA coatings

The angle between two relative prisms of the Vickers indenter was 136°. Vickers indenter was under 200 g load, and it was vertically pressed into the surface of the coatings to result in indentation, and the strength per unit area was Vickers hardness. In Fig. 11, the microhardness values of the bare P355GH steel and the No. 000, No. 001, No. 100, No. 101, No. 110, and No. 111 coatings under different working modes and shielding atmospheres were HV 480, 1209.45, 1172.72, 1306.02, 1247.84, 1368.38, and 1355.53 , respectively. The surface hardness of the structural steel surface was greatly improved, mainly due to the considerable proportion of Cr in the coating.

In X-ray diffraction, a beam of X-ray with a certain wavelength λ irradiated the polycrystalline surface, as shown in Fig. 12, and the maximum intensity of the reflected X-ray (i.e. diffraction peak) was obtained at a diffraction angle of 2θ. With d being the distance between the diffracting crystal planes, the diffraction follows Bragg's law [45]:

$$2d\sin\theta = n\cdot\lambda \tag{6}$$

As λ is known, the relationship between the macroscopic measurable diffraction angle 2θ and the microcrystal plane distance d could be established. When there is a stress σ in the coating, d must change with the orientation of the crystal plane and the stress. From our results, it is clear that the change in 2θ with the angle Ψ was closely related to σ, where Ψ is the angle between the normal of the sample surface and the crystal surface that diffracted X-rays. For isotropic polycrystalline

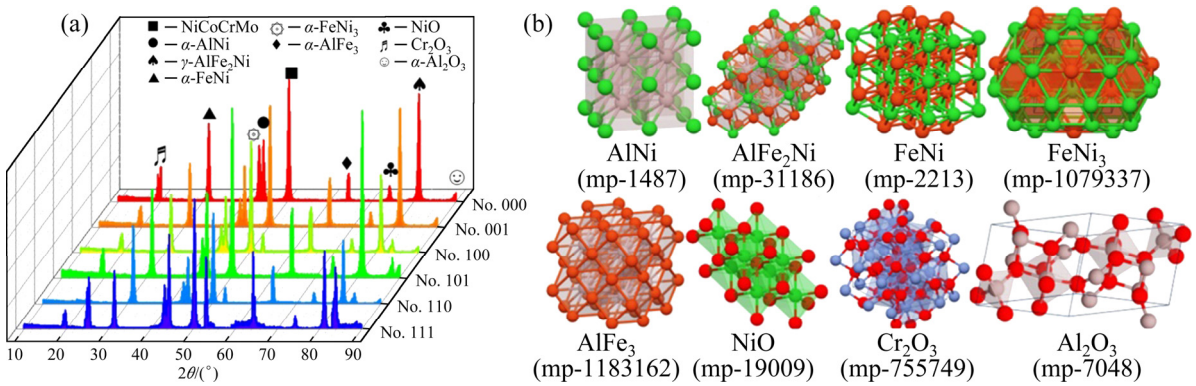

Fig. 10 XRD patterns (a) and phase structures of HEA coatings under different working modes and shielding atmospheres

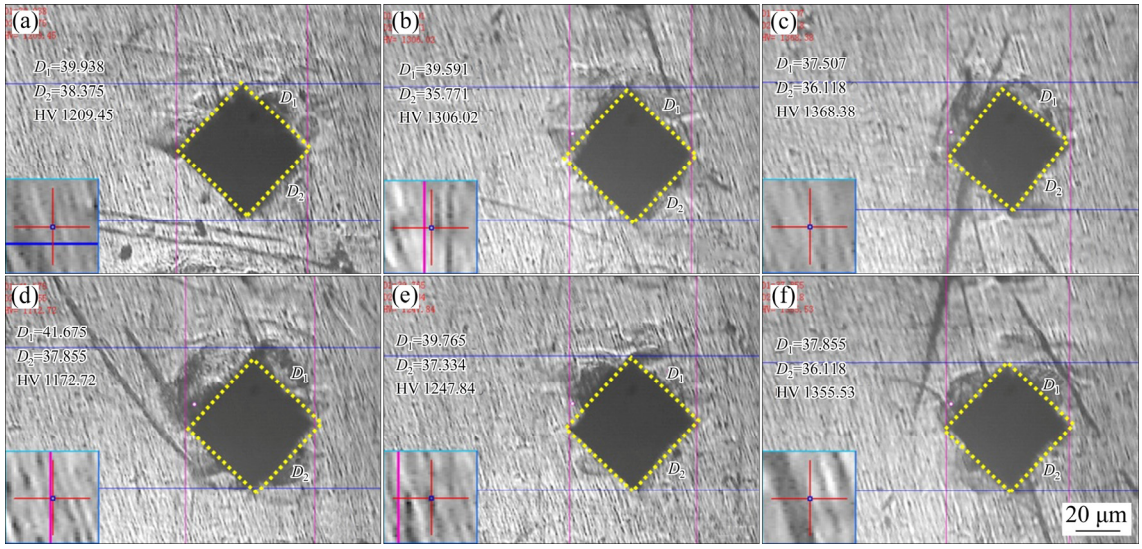

Fig. 11 Microhardness of HEA coatings under different working modes and shielding atmospheres: (a) No. 000; (b) No. 100; (c) No. 110; (d) No. 001; (e) No. 101; (f) No. 111

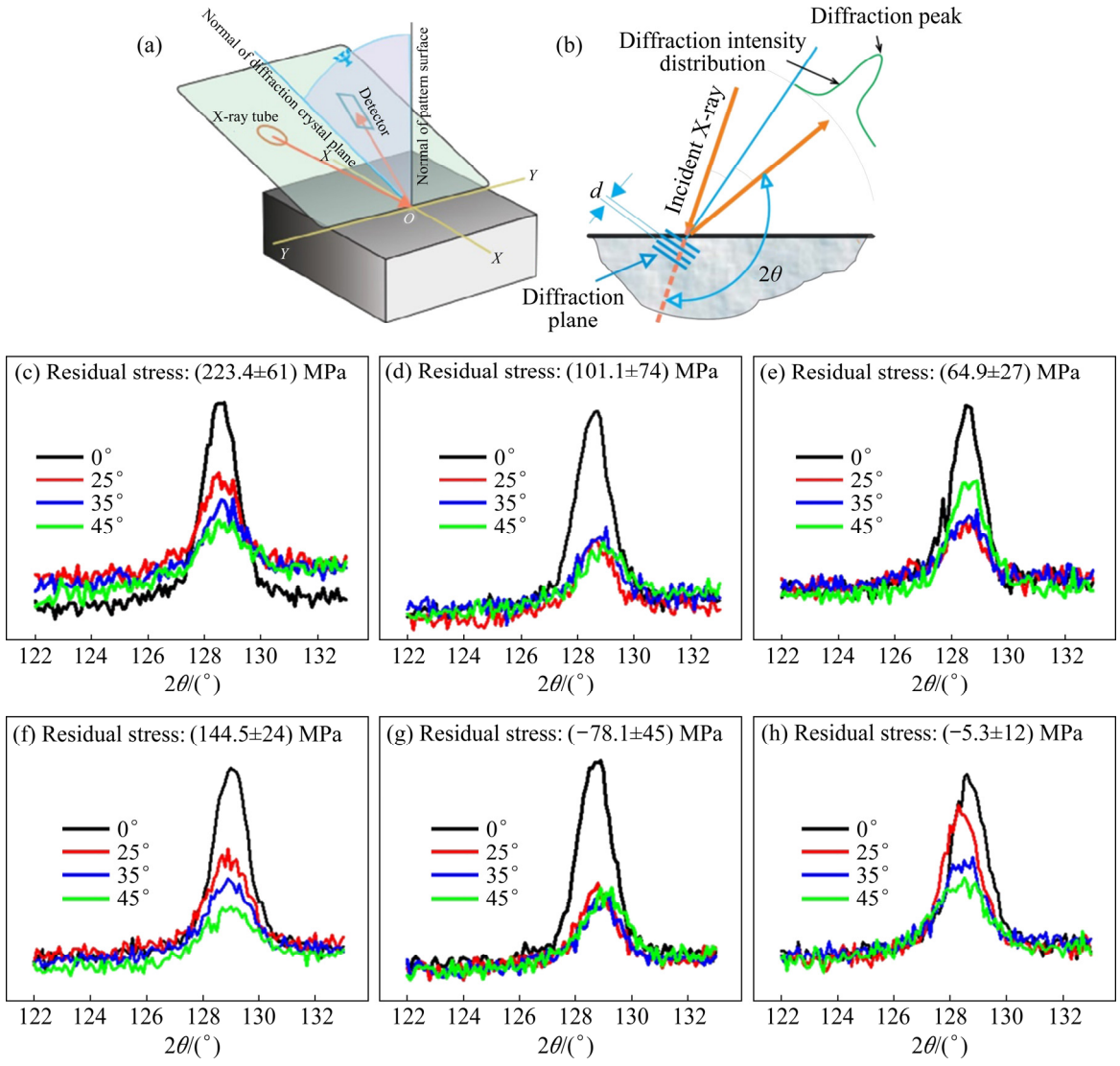

Fig. 12 X-ray diffraction stress measurement and residual stresses of HEA coatings: (a) Included angle, Ψ; (b) Measuring method; (c) No. 000; (d) No. 100; (e) No. 110; (f) No. 001; (g) No. 101; (h) No. 111

materials and in the plane stress state, σ is directly proportional to the slope of 2θ with $\sin^2\Psi$, and can be calculated according to Bragg's law and the elasticity theory:

$$\sigma=KM \tag{7}$$

$$M=\frac{\partial 2\theta}{\partial \sin^2\psi} \tag{8}$$

$$K=-\frac{E}{2(1+\nu)}\mathrm{ctg}\ \theta_0\cdot\frac{\pi}{180} \tag{9}$$

where K is the stress constant, E is elastic modulus, ν is Poisson's ratio, and θ_0 is the Bragg angle in a stress-free state.

The residual stress can be deduced from the theory of elasticity and X-ray diffraction [45]:

$$\sigma_f=\frac{-E}{2(1+\nu)}\mathrm{ctg}\,\theta_0\cdot\frac{\pi}{180}\frac{\partial(2\theta)}{\partial(\sin^2\psi)}-K\frac{\partial(2\theta)}{\partial(\sin^2\psi)} \tag{10}$$

The residual stress of the alloy coating fabricated by SLS mainly comprises (1) thermal stress that occurred when the coating was cooled from high temperature to room temperature, due to the uneven temperature distribution and difference in thermal expansion coefficients between the substrate and coatings and (2) intrinsic stress or internal stress caused by the non-thermal effect. The simulation results for temperature versus the stress–strain field are shown in Fig. 13. Because of the difference in the coefficient of thermal expansion between the coatings and P355GH, the residual stress generated in the coating (σ_{th}) can be described as follows [46,47]:

$$\sigma_{th}=\frac{E_c}{1-\nu_c}(\alpha_c-\alpha_s)(T_c-T_0) \tag{11}$$

where E_c is the elastic modulus of the coating, ν_c is Poisson's ratio of the coating, α_c (coatings) and α_s (P355GH) are the thermal expansion coefficients, and T_c and T_0 are the temperatures during coating preparation and measurement, respectively.

The maximum intrinsic stress (σ_{in}) can also be described as follows:

$$\sigma_{in}=CE_c\alpha_c(T_{cm}-T_s) \tag{12}$$

where T_{cm} and T_s are the melting point and substrate temperature, respectively, and C is a constant.

The residual stress (σ) of the coating is then the superposition of the coating thermal stress and substrate thermal stress:

$$\sigma=\sigma_{th}+\sigma_{in} \tag{13}$$

From the $2\theta_\psi$ vs $\sin^2\psi$ regression curves in Fig. 12, the residual stresses of No. 000, No. 100, No. 110, No. 001, No. 101, and No. 111 under different working modes and shielding atmospheres were (223.4±61), (101.1±74), (64.9±27), (144.5±24), (−78.1±45), and (−5.3±12) MPa, respectively. The diffraction peaks for the coating appeared at a 2θ of 127°−130° and the tensile stress showed elastic anisotropy, due to the inhomogeneous elastic deformation and non-uniform elastic−plastic deformation in the coatings, implying elastic and plastic anisotropy in the samples. The direction of principal stress matched that of the principal strain in the samples. Their partially nucleated phases were anisotropic, and the non-nucleated polycrystalline coatings presented pseudo-isotropy at the macroscopic level. Owing to the existence of residual stress in the coating, the thermal coupling effect in the coating was enhanced, which made it a sensitive factor contributing to the failure of the coating [48]. The residual stress in the coatings originated from the coating growth process and the storage environment. Its properties and magnitude were closely related to the substrate and coating materials, laser sintering technology,

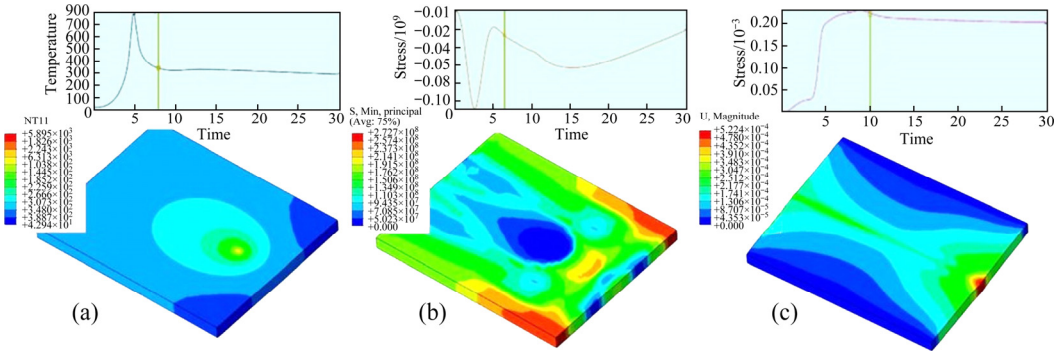

Fig. 13 Simulation of temperature and stress−strain field: (a) Temperature; (b) Stress; (c) Strain

conditions, and post-treatment process, and particularly, the effects of the different laser working modes and shielding atmospheres.

3.3.2 Bonding strength and stress−strain responses of HEA coatings

The interfacial bonding strength between the coating and P355GH steel was an important index for evaluating the process reliability of the coatings. In SLS, the internal stress caused by different thermal expansion coefficients of the HEA and steel significantly affected bonding strength. The elastic modulus, microhardness, and adhesion between the coating and steel were the main factors that determined bonding strength. The low value and sensitive nature of the elastic modulus indicated a bonding force between atoms, which also conformed to Hooke's law of elasticity [48]. Under normal stress, the elastic modulus was calculated as follows:

$$\sigma=E\cdot\varepsilon \tag{14}$$

where σ is the normal stress, and ε is the normal strain.

Under shear stress loading, the shear modulus was calculated using the following equation:

$$\tau=G\cdot\gamma \tag{15}$$

where τ is the shear stress, G is the shear modulus, and γ is the normal strain.

The relationship between E and G is expressed as

$$G=\frac{E}{2(1+\nu)} \tag{16}$$

The thermal stress of the coating was not greater than the bonding strength of the coatings, which indicated that the coating composition and SLS process inhibited any significant increase in the internal thermal stress. According to Fig. 14, the bonding strengths of No. 000, No. 001, No. 100, No. 101, No. 110, and No. 111 coatings using SLS with different laser working modes and shielding atmospheres were 40.45, 37.64, 45.87, 39.73, 51.71, and 46.94 MPa, respectively. The results indicated that higher elastic modulus led to higher bonding strength. In application, the bonding strength reflects the anti-elastic deformation ability of the HEA coatings. More importantly, the elastic deformation ability of the HEA coatings depends on the structure and interaction between atoms, which is affected by the laser-induced plasma. The

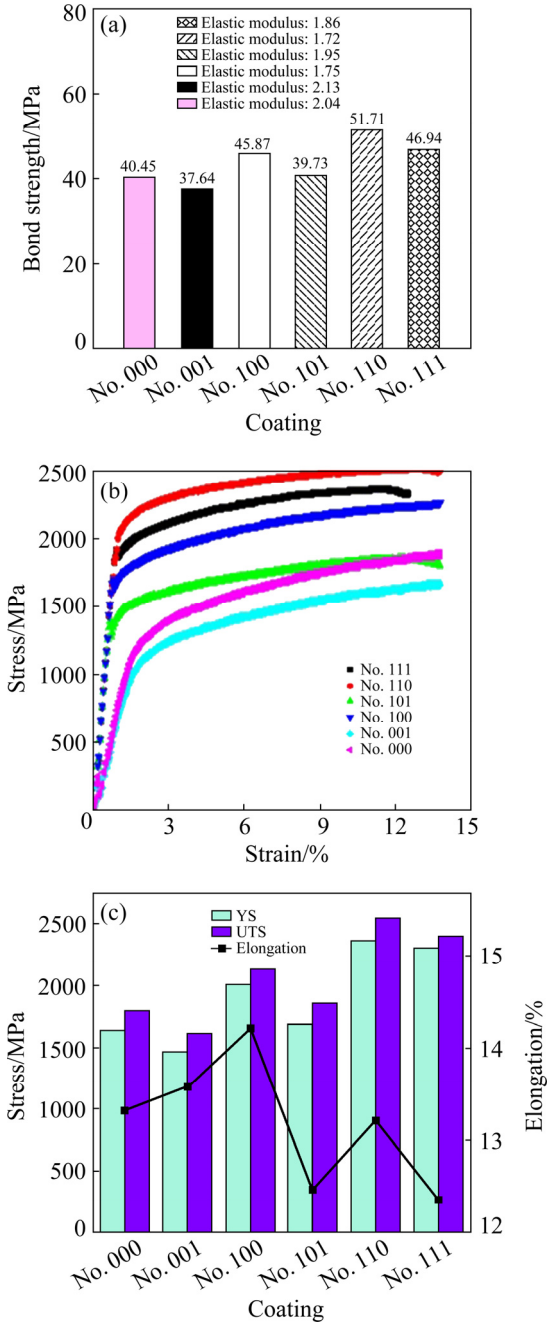

Fig. 14 Bonding strength and stress−strain responses of HEA coatings under different working modes and shielding atmospheres: (a) Bonding strength; (b) Stress−strain responses; (c) Mechanical properties

bonding strength of No. 110 coating under the pulsed laser working mode and Ar−He shielding atmosphere was noticeably higher than that of the coatings under other laser working modes and shielding atmospheres, owing to the suppression of the plasma shielding effect.

The tensile strength of the coating was analyzed by classical tensile testing, as shown in Fig. 14. KWEON et al [49] discovered that a typical

tensile test can reflect the real stress and strain before the necking point:

$$\sigma=S(1+s) \tag{17}$$

$$\varepsilon=\ln(1+s) \tag{18}$$

where S and s are the test stress and strain, respectively, and σ and ε are the real stress and strain, respectively.

In contrast, due to the stress triaxiality of the necking zone, the instantaneous real stress and strain values in the post-necking region should be calculated from the instantaneous load and cross-section as

$$\sigma=\frac{P}{A} \tag{19}$$

$$\varepsilon=\ln\left(\frac{A_0}{A}\right) \tag{20}$$

where P is the instantaneous load, and A_0 and A are the original and corresponding cross-sectional areas, respectively.

Since deformation during necking led to transverse stress at the necking region, an equivalent single-axis stress correction factor was set in this study. The factor was determined according to the pattern aperture, and was highly difficult to measure. Subsequently, the empirical function was calculated:

$$\sigma^s=B\sigma \tag{21}$$

$$B=0.0684(\lg\varepsilon)^3+0.0461(\lg\varepsilon)^2-0.205(\lg\varepsilon)+0.825\ (0.12\le\varepsilon\le3) \tag{22}$$

The stress–strain responses of the HEA coatings closely fitted the above empirical formula. The only deviation was a pseudo-random fluctuation in the elongation, where the elongation of No. 000 was higher than that of No. 001. This difference was mainly attributed to No. 000 and No. 001 coatings possessing microcrack defects in the surface layer. In contrast, the results of the fitting indicated that the mechanical properties of No. 110 and No. 111 coatings under the Ar−He shielding atmosphere were comparatively superior.

3.4 Friction and wear resistance

The surface friction curve and wear depths of the HEA coatings under a load of 10 N for 30 min are shown in Fig. 15. In the initial stage, the friction interaction between the coating and grinding ball occurred in the form of static friction and dynamic friction, and both the force and friction coefficient were greater in static friction than in dynamic friction. When the normal stress of friction exceeded the fatigue limit of the HEA coatings, the contact point was prone to plastic deformation, the oxide film on the coating surface was destroyed, and the interaction force between the HEA molecules increased at the contact point, resulting in cold welding, which mainly occurred in the samples of No. 101 and No. 111, as shown in Figs. 15(c, g). However, the phenomenon was significantly weaker in the samples of No. 100 and No. 110, as shown in Figs. 15(a, e). The dynamic friction coefficient μ reflects the friction and wear properties of the HEA coating, and there was a negative correlation between the wear resistance and the coefficient. The following equation describes the relationship among μ, the friction force f, and the positive pressure N:

$$\mu=f/N \tag{23}$$

As shown in Fig. 16, the stable friction coefficients (μ) of No. 100, No. 101, No. 110, and No. 111 alloy coatings by SLS under different working modes and shielding atmospheres were 0.156, 0.201, 0.106, and 0.143, and the corresponding friction forces (f) were 1.553, 2.008, 1.058, and 1.427 N, respectively.

The above mechanical analysis and friction and wear experiments were more convincing. Whether evaluating through simulation, mechanical experiment, or friction behavior analysis, or from a macro or micro point of view, the different laser working modes and shielding atmospheres had significant effects on the properties of the HEA coatings fabricated using SLS, particularly impacting the shielding effect of the laser-induced plasma on SLS.

4 Conclusions

(1) The appearance and disappearance of some typical spectral features indicated that the state of the plasma plume in SLS was affected by the working mode and shielding atmosphere, and the emission intensity decreased in the pulsed laser working mode and Ar−He shielding gas environment.

(2) T_e and the jet volume of plasma in He gas

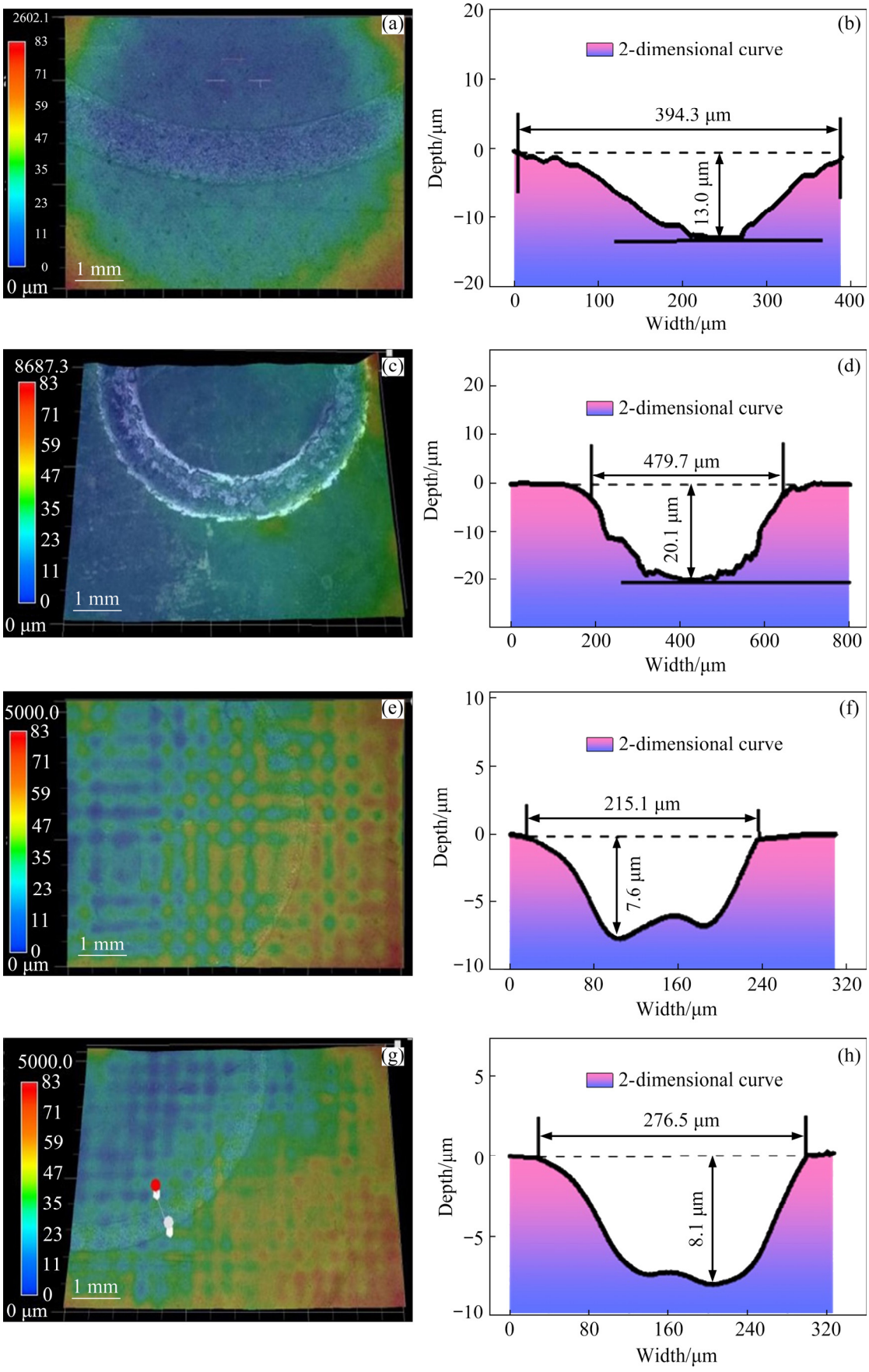

Fig. 15 Morphologies and profiles of wear depths: (a, b) No. 100; (c, d) No. 101; (e, f) No. 110; (g, h) No. 111

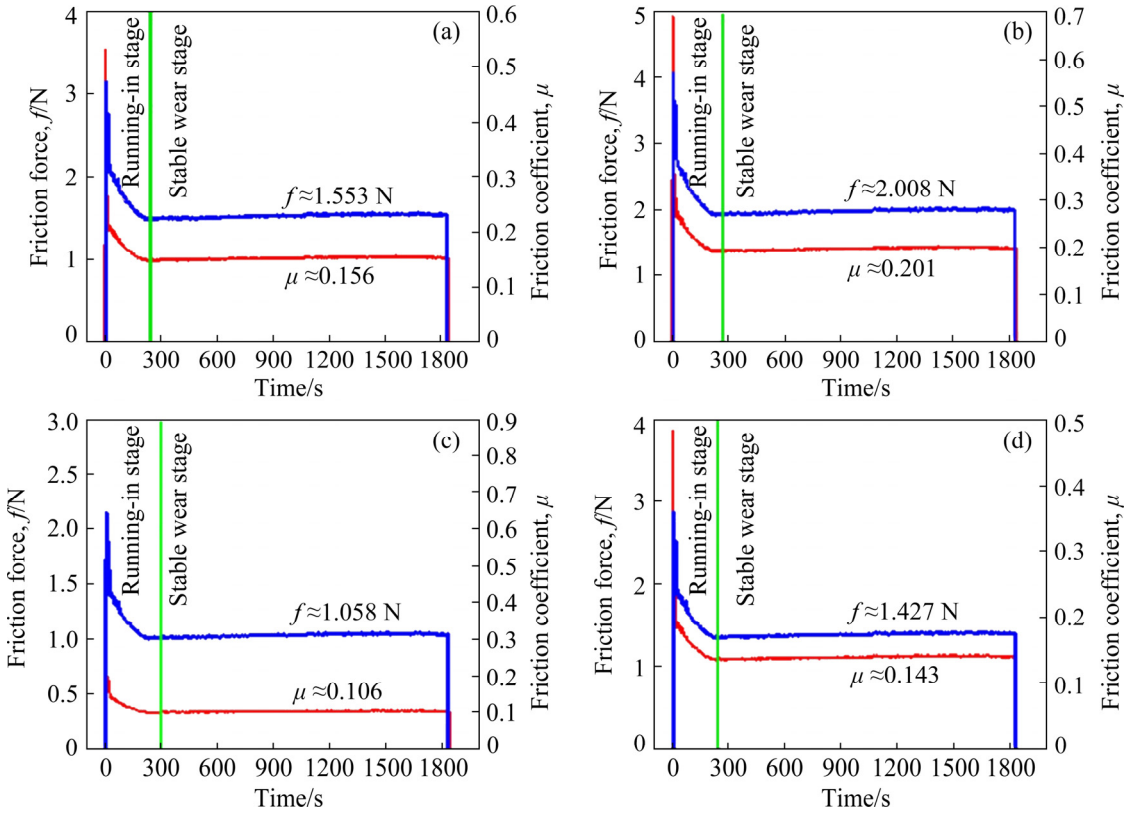

Fig. 16 Friction curve of HEA coatings: (a) No. 100; (b) No. 101; (c) No. 110; (d) No. 111

were higher than those in Ar−He gas, which indicated that the shielding effect was induced by SLS in the following order: no shielding gas > He shielding gas > Ar−He shielding gas.

(3) During laser scanning, there was a noticeable thermal accumulation superposition effect and it reached the latent heat of liquefaction under the action of long-time pulse pumping. Marked phase transitions and diffusion as well as metallurgical bonding occurred, with the precipitation of α-$AlFe_3$, NiCoCrMo, α-AlNi, and γ-$AlFe_2Ni$.

(4) The residual stress and dynamic friction coefficient of the coating could be respectively reduced to −5.3 MPa and 1.058 by changing the laser working mode and shielding atmosphere, which suppressed the shielding effect of the laser-induced plasma on the SLS process.

Acknowledgments

This work was supported by the Natural Science Foundation of Jiangsu Province, China (No. BK20191036), and Foundation of Research Project of China (No. JCKY 61420051911).

References

[1] LUREAU F, MATRAS G, CHALUS O, DERYCKE C, MORBIEU T, RADIER C, CASAGRANDE O, LAUX S, RICAUD S, REY G, PELLEGRINA A, RICHARD C, BOUDJEMAA L, SIMON-BOISSON C, BALEANU A, BANICI R, GRADINARIU A, CALDARARU C, de BOISDEFFRE B, GHENUCHE P, NAZIRU A, KOLLIOPOULOS G, NEAGU L, DABU R, DANCUS I, URSESCU D. High-energy hybrid femtosecond laser system demonstrating 2 x 10 PW capability [J]. High Power Laser Science and Engineering, 2020, 8: e43.

[2] ZHANG Zong-xin, WU Fen-xiang, HU Jia-bing, YANG Xiao-jun, GUI Jia-yan, JI Peng-hua, LIU Xing-yan, WANG Cheng, LIU Yan-qi, LU Xiao-ming, XU Yi, LENG Yu-xin, LI Ru-xin, XU Zhi-zhan. The 1 PW/0.1 Hz laser beamline in SULF facility [J]. High Power Laser Science and Engineering, 2020, 8: e4.

[3] CHENG Zhuo, YANG Lu, MAO Wen-hao, HUANG Zhi-kun, LIANG Ding-shan, HE Bin, REN Fu-zeng. Achieving high strength and high ductility in a high-entropy alloy by a combination of a heterogeneous grain structure and oxide-dispersion strengthening [J]. Materials Science and Engineering A−Structural Materials Properties Microstructure and Processing, 2021, 805: 140544.

[4] TRAVERSIER M, MESTRE-RINN P, PEILLON N, RIGAL E, BOULNAT X, TANCRET F, DHERS J,

FRACZKIEWICZ A. Nitrogen-induced hardening in an austenitic CrFeMnNi high-entropy alloy (HEA) [J]. Materials Science and Engineering A−Structural Materials Properties Microstructure and Processing, 2021, 804: 14072.

[5] ZHAO Wen-rui, HAN J K, KUZMINOVA Y O, EVLASHIN S A, ZHILYAEV A P, PESIN A M, JANG J I, LISS K D, KAWASAKI M. Significance of grain refinement on micro-mechanical properties and structures of additively-manufactured CoCrFeNi high-entropy alloy [J]. Materials Science and Engineering A−Structural Materials Properties Microstructure and Processing, 2021, 807: 140898.

[6] LI Dong-yue, LI Cheng-xin, FENG Tao, ZHANG Yi-dong, SHA Gang, LEWANDOWSKI J J, LIAW P K, ZHANG Yong. High-entropy Al0.3CoCrFeNi alloy fibers with high tensile strength and ductility at ambient and cryogenic temperatures [J]. Acta Materialia, 2017, 123: 285−294.

[7] OTTO F, DLOUHÝ A, SOMSEN C, BEI H, EGGELER G, GEORGE E P. The influences of temperature and microstructure on the tensile properties of a CoCrFeMnNi high-entropy alloy [J]. Acta Materialia, 2013, 61: 5743−5755.

[8] ZHANG Li-song, ZHANG Xiao-nan, LI Na, MEI Xian-xiu, LI Xiao-na, WANG You-nian, CAO Xing-zhong, PAVLOV S K, REMNEV G E, UGLOV V V, LU Er-yang. Study on thermal shock irradiation resistance of CoCrFeMnNi high entropy alloy by high intensity pulsed ion beam [J]. Journal of Nuclear Materials, 2022, 559: 153413.

[9] ZHANG Wei-ran, LIAW P K, ZHANG Yong. Science and technology in high-entropy alloys [J]. Science China Materials, 2018, 61(1): 2−22.

[10] FU Peng-huai, WANG Nan-qing, LIAO Hai-guang, XU Wen-yu, PENG Li-ming, CHEN Juan, HU Guo-qi, DING Wen-jiang. Microstructure and mechanical properties of high strength Mg−15Gd−1Zn−0.4Zr alloy additive-manufactured by selective laser melting process [J]. Transactions of Nonferrous Metals Society of China, 2021, 31: 1969−1978.

[11] ZENG Min, YAN Hong, YU Bao-biao, HU Zhi. Microstructure, microhardness and corrosion resistance of laser cladding Ni−WC coating on AlSi5Cu1Mg alloy [J]. Transactions of Nonferrous Metals Society of China, 2021, 31: 2716−2728.

[12] HAN Li-ying, WAN Cun-shan. Microstructure and properties of Ti64.51Fe26.40Zr5.86Sn2.93Y0.30 biomedical alloy fabricated by laser additive manufacturing [J]. Transactions of Nonferrous Metals Society of China, 2020, 30: 3274−3286.

[13] LIN Wei, CHEN Di-han, CHEN S C. Emerging micro-additive manufacturing technologies enabled by novel optical methods [J]. Photonics Research, 2020, 8(12): 1827−1842.

[14] JIANG Tong, GAO Si, TIAN Zhen-nan, ZHANG Han-zhuang, NIU Li-gang. Fabrication of diamond ultra-fine structures by femtosecond laser [J]. Chinese Optics Letters, 2020, 18(10): 42−46.

[15] SULMONI L, MEHNKE F, MOGILATENKO A, GUTTMANN M, WERNICKE T, KNEISSL M. Electrical properties and microstructure formation of V/Al-based n-contacts on high Al mole fraction n-AlGaN layers [J], Photonics Research, 2020, 8(8): 1381−1387.

[16] QIAN Jing, WANG Guan-de, LOU Kong-yu, SHEN Dan-yang, FU Qiang, ZHAO Quan-zhong. Self-induced birefringence of white-light continuum generated by interaction of focused femtosecond laser pulses with fused silica [J]. High Power Laser Science and Engineering, 2020, 8, e19.

[17] AIZENSHTEIN M, PRIEL E, HAYUN S. Effect of pre-deformation and B2 morphology on the mechanical properties of Al0.5CoCrFeNi HEA [J]. Materials Science and Engineering A−Structural Materials Properties Microstructure and Processing, 2020, 788: 139575.

[18] ERDOGAN A, DOLEKER K M. Comparative study on dry sliding wear and oxidation performance of HVOF and laser re-melted Al0.2CrFeNi(Co,Cu) alloys [J]. Transactions of Nonferrous Metals Society of China, 2021, 31: 2428−2441.

[19] GERA D, SANTOS J, KIMINAMI C S, GARGARELLA P. Comparison of Cu–Al–Ni–Mn–Zr shape memory alloy prepared by selective laser melting and conventional powder metallurgy [J]. Transactions of Nonferrous Metals Society of China, 2020, 30: 3322−3332.

[20] ZHANG Dong-hui, KONG De-jun. Microstructures and immersion corrosion behavior of laser thermal sprayed amorphous Al−Ni coatings in 3.5% NaCl solution [J]. Journal of Alloys and Compounds, 2017, 735: 1−12.

[21] PICOLLO F, RUBANOV S, TOMBA C, BATTIATO A, ENRICO E, PERRAT-MABILON A, PEAUCELLE C, THI T N T, BOARINO L, GHEERAERT E, OLIVERO P. Effects of high-power laser irradiation on sub-superficial graphitic layers in single-crystal diamond [J]. Acta Materialia, 2016, 103: 665−671.

[22] GUO Meng, HE Hong-bo, YI Kui, SHAO Shu-ying, HU Guo-hang, SHAO Jian-da. Optical characteristics of ultrathin amorphous Ge films [J]. Chinese Optics Letters, 2020, 18(10): 82−86.

[23] TAKABE H, KURAMITSU Y. Recent progress of laboratory astrophysics with intense lasers [J]. High Power Laser Science and Engineering, 2021, 9: e49.

[24] WANG Xiang-Bing, HU Guang-Yue, ZHANG Zhi-Meng, GU Yu-Qiu, ZHAO Bin, ZUO Yang, ZHENG Jian. Gamma-ray generation from ultraintense laser-irradiated solid targets with preplasma [J]. High Power Laser Science and Engineering, 2020, 8: e36.

[25] LUO Yi, ZHU Liang, HAN Jing-tao, XIE Xiao-jian, WAN Rui, ZHU Yang. Study on the acoustic emission effect of plasma plume in pulsed laser welding [J]. Mechanical Systems and Signal Processing, 2019, 124: 715−723.

[26] WU Yue, CAI Yan, SUN Da-wei, ZHU Jun-jie, WU Yi-xiong. Characteristics of plasma plume and effect mechanism of lateral restraint during high power CO_2 laser welding process [J]. Optics and Laser Technology, 2014, 64: 72−81.

[27] ZHANG Yi, LI Fa-zhi, LIANG Zhi-chao, YING Ye-yong, LIN Qi-da, WEI Hai-ying. Correlation analysis of penetration based on keyhole and plasma plume in laser

welding [J]. Journal of Materials Processing Technology, 2018, 256: 1−12.

[28] JIANG Meng, TAO Wang, WANG Shu-liang, LI Li-qun, CHEN Yan-bin. Effect of ambient pressure on interaction between laser radiation and plasma plume in fiber laser welding [J]. Vacuum, 2017, 138: 70−79.

[29] YANG Sha-sha, YANG Lan-lan, CHEN Ming-hui, WANG Jin-long, ZHU Sheng-long, WANG Fu-hui. Understanding of failure mechanisms of the oxide scales formed on nanocrystalline coatings with different Al content during cyclic oxidation [J]. Acta Materialia, 2021, 205: 116576.

[30] TANG En-ling, HE Zhen-hui, CHEN Chuang, HAN Ya-fei. Characterization of dynamic compressive strength and impact release energy of Al/PTFE energetic materials reinforced by aluminum honeycomb skeleton [J]. Composite Structures, 2020, 241: 112063.

[31] BAI Li, LIU Yun-zi, GUO Yang-yang, LV Yu-kun, GUO Ting-ting, CHEN Jian. Effects of Al addition on microstructure and mechanical properties of Co-free $(Fe40Mn40Ni10Cr10)_{100-x}Al_x$ high-entropy alloys [J]. Journal of Alloys and Compounds, 2021, 879: 160342.

[32] ZHANG Yong, ZUO Ting-ting, ZHI Tang, GAO M C, DAHMEN K A, LIAW P K, LU Zhao-ping. Microstructures and properties of high-entropy alloys [J]. Progress in Materials Science, 2014, 61: 1−93.

[33] CANTOR B, CHANG I T H., KNIGHT P, VINCENT A J B. Microstructural development in equiatomic multicomponent alloys [J]. Materials Science and Engineering A−Structural Materials Properties Microstructure and Processing, 2004, 375/376/377: 213−218.

[34] GEORG S, HENRIK L, STEPHAN B, CHRISTIAN P, ABDULLAH R, VOLKMAR S, ARMIN S, HERMANN S. Heat accumulation during femtosecond laser treatment at high repetition rate — A morphological, chemical and crystallographic characterization of self-organized structures on Ti6Al4V [J]. Applied Surface Science, 2021, 570: 151115.

[35] SU Chen-yi, SHEN Bing-lin, XU Xing-qi, XIA Chun-sheng, PAN Bai-liang. Simulation and analysis of the time evolution of laser power and temperature in static pulsed XPALs [J]. High Power Laser Science and Engineering, 2019, 7: e44.

[36] ZHU Guo, SUN Jiang-ping, GUO Xiong-xiong, ZOU Xi-xi, ZHANG Li-bin, GAN Zhi-yin. Molecular dynamics simulation of temperature effects on low energy near-surface cascades and surface damage in Cu [J]. Nuclear Instruments and Methods in Physics Research Section B: Beam Interactions with Materials and Atoms, 2017, 401: 45−50.

[37] REISGEN U, SCHLESER M, MOKROV O, AHMED E. Shielding gas influences on laser weldability of tailored blanks of advanced automotive steels [J]. Applied Surface Science, 2010, 257: 1401−1406.

[38] XU Jie, LUO Yi, ZHU Liang, HAN Jing-tao, CHEN Dong. Effect of shielding gas on the plasma plume in pulsed laser welding [J]. Measurement, 2019, 134: 25−32.

[39] YANG Q, KALATHIPARAMBIL K, ELG D T, RUZIC D, KRIVEN W M. Microstructural damage of α-Al_2O_3 by high energy density plasma [J]. Acta Materialia, 2017, 132: 479−490.

[40] MANZOOR A W, VISHAL T, HARJIT S G, NITI K. Effect of axial electron temperature and plasma density ramp on self-focusing/defocusing of a laser beam in plasma [J]. Laser Physics, 2014, 24(10): 106003.

[41] USPENSKIY S A, SHCHEGLOV P Y, PETROVSKIY V N, GUMENYUK A V, RETHMEIER M. Spectral diagnostics of a vapor-plasma plume produced during welding with a high-power ytterbium fiber laser [J]. Optics and Spectroscopy, 2015, 594: 012033.

[42] KAWAHITO Y, MATSUMOTO N, MIZUTANI M, KATAYAMA S. Characterization of plasma induced during high power fiber laser welding of stainless steel [J]. Science and Technology of Welding and Joining, 2008, 13: 744−748.

[43] CLAVE E, GAFT M, MOTTO-ROS V, FABRE C, FORNI O, BEYSSAC O, MAURICE S, WIENS R C, BOUSQUET B. Extending the potential of plasma-induced luminescence spectroscopy [J]. Spectrochimica Acta Part B: Atomic Spectroscopy, 2021, 177: 106111.

[44] ZHANG YUE, WANG FENG, LIU Jian-yong, SUN Ji-zhong. Simulation of the inverse bremsstrahlung absorption by plasma plume in laser penetration welding [J]. Chemical Physics Letters, 2022, 793: 139434.

[45] WANG Wen-rui, YUAN Li-hong, LI Yun, YANG Meng-yao, ZHANG Hui, ZHANG Wang-feng. Test method for residual stress analysis of the inner surface of small caliber Ti−3Al−2.5V tubing by X-ray diffraction [J]. Vacuum, 2020, 177: 109371.

[46] SLIM M F, ALHUSSEIN A, ZGHEIB E, FRANCOIS M. Determination of single-crystal elasticity constants of the beta phase in a multiphase tungsten thin film using impulse excitation technique, X-ray diffraction and micro-mechanical modeling [J]. Acta Materialia, 2019, 175: 348−360.

[47] HEMMESI K, FARAJIAN M, BOIN M. Numerical studies of welding residual stresses in tubular joints and experimental validations by means of X-ray and neutron diffraction analysis [J]. Materials & Design, 2017, 126: 339−350.

[48] ZHANG Dong-hui, KONG De-jun. Surface and cross-section characteristics and immersion corrosion behavior of laser thermal sprayed amorphous $AlNiCoCrY_2O_3$ coatings [J]. Applied Surface Science, 2018, 457: 69−82.

[49] KWEON H D, KIM J W, SONG O, OH D. Determination of true stress-strain curve of type 304 and 316 stainless steels using a typical tensile test and finite element analysis [J]. Nuclear Engineering and Technology, 2020, 53(2): 647−656.

等离子体控制优化激光烧结 $Ni_{30}Cr_{25}Al_{15}Co_{15}Mo_5Ti_5Y_5$ 高熵合金涂层的显微组织与性能

颜 雪[1]，徐健晏[2]，管相合[3]，韩冰源[4]，张 诚[1]，崔自若[5]，梁文萍[2]

1. 中国科学院 上海光学精密机械研究所 强场激光物理国家重点实验室，上海 201800；
2. 南京航空航天大学 材料科学与技术学院，南京 211106；
3. 中国工程物理研究院 上海激光等离子体研究所，上海 201800；
4. 江苏理工学院 汽车与交通工程学院，常州 213001；
5. 上海交通大学 物理与天文学院 IFSA 协同创新中心(CICIFSA)
激光等离子体教育部重点实验室，上海 200240

摘 要：提出一种激光诱导等离子体的主动抑制方法，以优化 $Ni_{30}Cr_{25}Al_{15}Co_{15}Mo_5Ti_5Y_5$ 高熵合金(HEA)涂层表面激光烧结(SLS)的晶体结构和摩擦学性能，该过程采用脉冲激光和不同保护气体。结果表明，无保护气体或 He 气氛下的电子温度(T_e)和等离子体射流体积均高于 Ar−He 气氛下的。SLS 过程中发生明显的相变和金属原子扩散，α-$AlFe_3$、α-AlNi 和 γ-$AlFe_2Ni$ 化合物沉淀形成冶金结合。等离子体通过逆韧致辐射(IB)吸收较低能量加强激光与 HEA 之间的相互作用，使涂层显微硬度增加，动态摩擦因数降低，这说明等离子体控制对激光增材制造存在重要影响。

关键词：激光诱导等离子体；表面激光烧结；电子温度；逆韧致辐射吸收；高熵合金；残余应力

(Edited by Bing YANG)